Homotopy scattering series for seismic forward modelling with variable density and velocity

Kui Xiang[1]*, Kjersti Solberg Eikrem[2], Morten Jakobsen[1,2] and Geir Nævdal[2]

[1]*Department of Earth Science, University of Bergen, Postboks, Bergen, 7803 5020, Norway, and* [2]*NORCE Norwegian Research Centre AS, Postboks 22 Nygårdstangen, Bergen, 5838, Norway*

ABSTRACT

We have derived a convergent scattering series solution for the frequency-domain wave equation in acoustic media with variable density and velocity. The convergent scattering series solution is based on the homotopy analysis of a vectorial integral equation of the Lippmann–Schwinger type. By using the Green's function and partial integration, we have derived the vectorial integral equation of the Lippmann–Schwinger type that involves the pressure gradient field as well as the pressure field from the wave equation. The vectorial Lippmann–Schwinger equation can in principle be solved via matrix inversion, but the computational cost of matrix inversion scales like N^3, where N is the number of grid blocks. The computational cost can be significantly reduced if one solves the vectorial Lippmann–Schwinger equation iteratively. A simple iterative solution is the Born series, but it is only convergent when the scattering potential is sufficiently small. In this study, we have used the so-called homotopy analysis method to derive an iterative solution for the vectorial Lippmann–Schwinger equation which can be made convergent even in strongly scattering media. The computational cost of our convergent scattering series scales as N^2. Our algorithm, which is based on the homotopy analysis method, involves a convergence control operator that we select using hierarchical matrices. We use a three-layer model and a resampled version of the SEG/EAGE salt model to show the performance of the developed convergent scattering series.

Key words: Density and velocity, Forward modelling, Series solution.

INTRODUCTION

The integral equation method is one of the most valuable methods in seismic forward modelling and inversion (Aki and Richards, 1980; Van Den Berg and Kleinman, 1997; Carcione *et al.*, 2002; Abubakar *et al.*, 2003; Innanen, 2009; Jakobsen, 2012; Jakobsen and Ursin, 2015; Malovichko *et al.*, 2018; Huang *et al.*, 2020). It considers the total wavefield in the actual medium as a superposition of a background wavefield and a scattering wavefield. The background wavefield and the scattering wavefield are found from the integral representations in terms of the Green's function and the actual and vir-

tual source. The virtual source is caused by the contrast between the actual medium and the background medium. If the contrast part is compact enough, the computation will be accelerated. Although the integral equation system matrix is relatively small due to the compact contrast part, it is still a full matrix. If we implement it through matrix inversion, it will cause a relatively high memory demand and computational burden (Jakobsen and Wu, 2018), especially when the model is a large-scale model. This fact leads researchers to use iterative methods based on scattering series solutions instead of direct matrix inversion for solving the integral equation. One of the most well-known series solutions in the geophysical community is the Born series solution (Morse and Feshbach, 1954). However, the conventional Born series is only
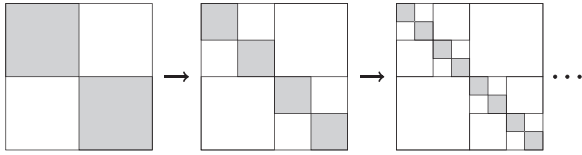
*E-mail: Kui.Xiang@uib.no

Figure 1 The construction of a hierarchical matrix. This type of hierarchical matrix is called hierarchically off-diagonal low rank (HODLR).
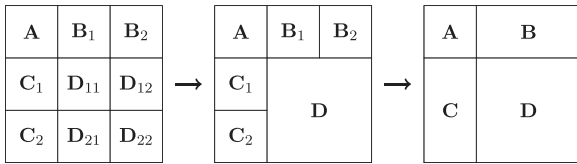

Figure 2 The construction of hierarchical $\mathbf{I} - \mathbf{G}^{(0)}\mathbf{V}$.

guaranteed to converge when the contrast or the scattering potential of the model is relatively small (Jakobsen and Ursin, 2015; Osnabrugge *et al.*, 2016). Therefore, a lot of effort has been devoted to solving the divergence problem of the Born series in the presence of strong contrasts. Zhdanov and Fang (1997) have generalized the Born series by using the higher order quasi-linear approximations to ensure the modified series converge to the true solution. Osnabrugge *et al.* (2016) have modified the Born series to converge for high scattering potentials by introducing a pre-conditioner and an auxiliary parameter to localize the energy of the Green's function. Jakobsen and Wu (2016) have replaced the Born series with a convergent renormalized scattering series by utilizing the leading De Wolf approximation. By using the modified volume integral equation proposed by Bonnet and others (2017), Abhishek *et al.* (2020) have developed a modified Born series, that is unconditionally convergent, for the forward and inverse scattering problem.

All the methods mentioned above assume that the density is constant. But in fact density plays an important role in the amplitude of the wavefield. If we only consider the velocity in wavefield forward modelling when density varies in reality, the synthetic seismic wavefield will not match the observed wavefield well, which may cause serious artefacts in the full wave-

form inversion (Virieux and Operto, 2009). Many forward modelling methods, most of them for the ultrasound imaging, have been developed with variable density (Kwon and Jeong, 1998; Lavarello and Oelze, 2009; Mojabi and LoVetri, 2015; Rao *et al.*, 2020). In recent years, some studies about integral equation methods for seismic forward modelling with variable density have been considered in several publications (Yang *et al.*, 2016; Yao *et al.*, 2016; Sun *et al.*, 2017; Jiménez *et al.*, 2018; Luo and Wu, 2018; Farshad and Chauris, 2020). Although these studies have been developed, there is still an important need to develop more accurate and efficient methods for seismic forward modelling with variable density. Therefore, in this study, we present a new integral equation scheme applicable in the case of variable density and velocity.

Unlike other seismic forward modelling methods that include density and velocity, we have derived two coupled integral equations and combined them into a vectorial Lippmann–Schwinger (LS) equation. Because there are already many methods for solving the LS equation (Jakobsen and Ursin, 2015; Jakobsen and Wu, 2016; Eftekhar *et al.*, 2018; Huang *et al.*, 2020; Eikrem *et al.*, 2020), we may use those methods to solve the vectorial LS equation. This is our main motivation to extend the previous methods to the variable velocity and density case. Because of the introduction of the density term, the scattering potential involving two parameters in the vectorial LS equation becomes complicated. It is necessary to further develop a convergent scattering series solution for the vectorial LS equation due to the strong scattering potential. In this study, we use the homotopy analysis method developed by Liao (1997, 2003), and Liao and Tan (2007) to solve the vectorial LS equation. There have been many successful applications of the homotopy techniques in geophysics. Keller and Perozzi (1983) introduced continuation in their methods for fast seismic ray tracing. Hanyga and Pajchel (1995) further explored homotopy methods in complicated models. Allgower and Georg (1990) give an introduction to numerical homotopy methods. Huang and Greenhalgh (2018) used the modern homotopy analysis method (Liao, 2003) to solve anisotropic eikonal equation for traveltime approximations. Jakobsen *et al.* (2020) have proposed a convergent

Table 1 Levels and ranks for constructing the hierarchical matrix for different models and frequencies

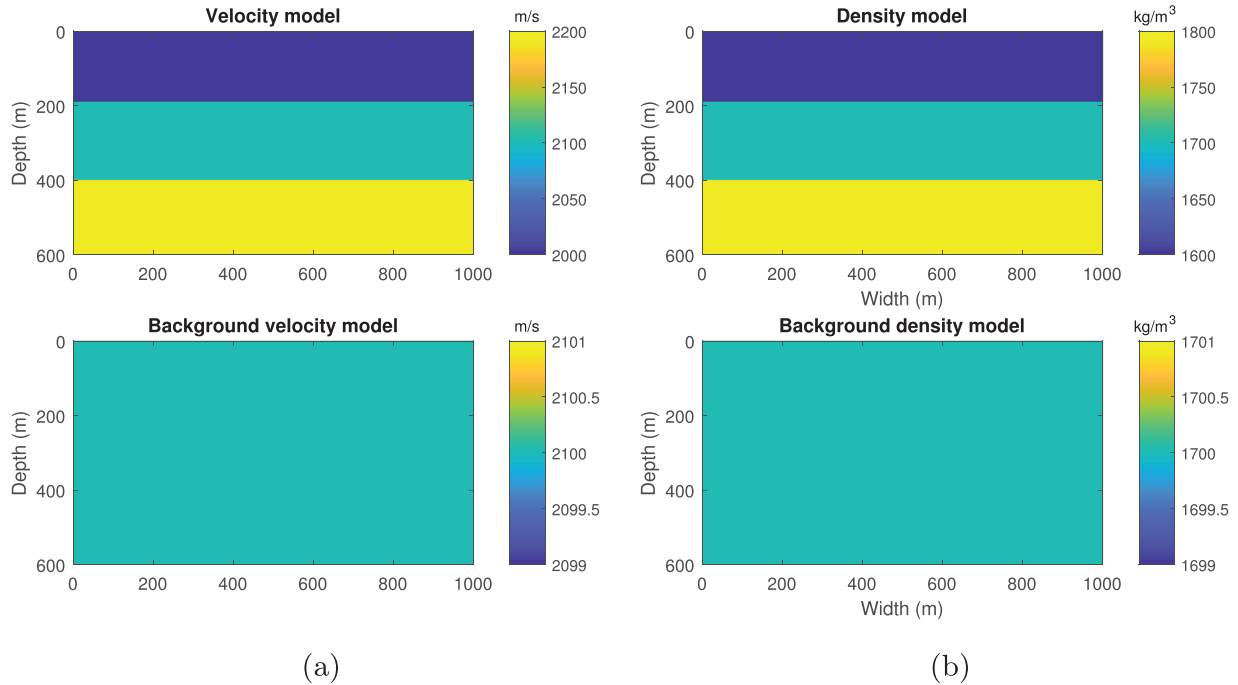|	The three-layer model			The resampled SEG/EAGE salt model		
Frequency	5 Hz	20 Hz	40 Hz	5 Hz	20 Hz	40 Hz
Level	4	4	3	4	3	3
Rank 1	10	20	60	10	60	120
Rank 2	5	10	30	5	30	120

(a)   (b)

Figure 3 The three-layer model and its background model.

scattering series solution of the scalar LS equation through the homotopy analysis method. Jakobsen *et al.* (2020) have compared convergence performance of different scattering series derived from homotopy continuation method and renormalization group. Previously, Jakobsen *et al.* (2020) have concluded that the scattering series solution is guaranteed to converge in fixed density case by introducing a suitable convergence control operator. In the present study, we modify the homotopy analysis method in Jakobsen *et al.* (2020) to solve the vectorial LS equation. Due to the strong scattering potential in the vectorial LS equation, the simple convergence control operator given in Jakobsen *et al.* (2020) cannot ensure that the scattering series converges. So we introduced another convergence control operator developed by Eikrem *et al.* (2020) based on the matrix low rank approximation (Halko *et al.*, 2011) and the hierarchical matrix (Börm *et al.*, 2003). In Eikrem *et al.* (2020), they mainly focus on the convergence control operator for the scalar LS equation. In this study, we developed a new convergence control operator for the vectorial LS equation based on Eikrem *et al.* (2020) by constructing hierarchical matrices for different blocks of the full matrix. In principle, if we choose the parameters related to the convergence control operator properly, the homotopy scattering series will converge.

This paper is structured as follows. First we transform the wave equation for acoustic medium into the vectorial integral equation of the LS type. Then we discuss the reference solution from matrix inversion as well as the conventional Born series solution. Next we give a description of the homotopy analysis method and derive the convergent homotopy series solution. Finally we use numerical examples to demonstrate the performance of the proposed method, compare it with the conventional Born series and give the concluding remarks. The formulation of two-dimensional and three-dimensional acoustic Green's functions and their spatial derivatives are given in Appendices A and B.

THEORY

The vectorial Lippmann–Schwinger equation

The acoustic wave equation for heterogeneous medium in frequency domain can be written as (Červený, 2005)

$$\left(\nabla \cdot \frac{1}{\rho(\mathbf{x})}\nabla + \frac{\omega^2}{\kappa(\mathbf{x})}\right)p(\mathbf{x}, \omega) = -S(\mathbf{x}, \omega), \tag{1}$$

where ∇ is the spatial gradient operator, ω is the angular frequency, $\kappa(\mathbf{x}) = \rho(\mathbf{x})v^2(\mathbf{x})$ is the bulk modulus related to the density $\rho(\mathbf{x})$ and the velocity $v(\mathbf{x})$, $p(\mathbf{x}, \omega)$ is the pressure wavefield in the acoustic medium and $S(\mathbf{x}, \omega)$ represents the source term, $\mathbf{x} \in \mathbb{R}^n$ is the spatial position, where $n = 2, 3$ denotes the dimensionality of the problem. The wavefield p, the source term S and the following Green's functions are all
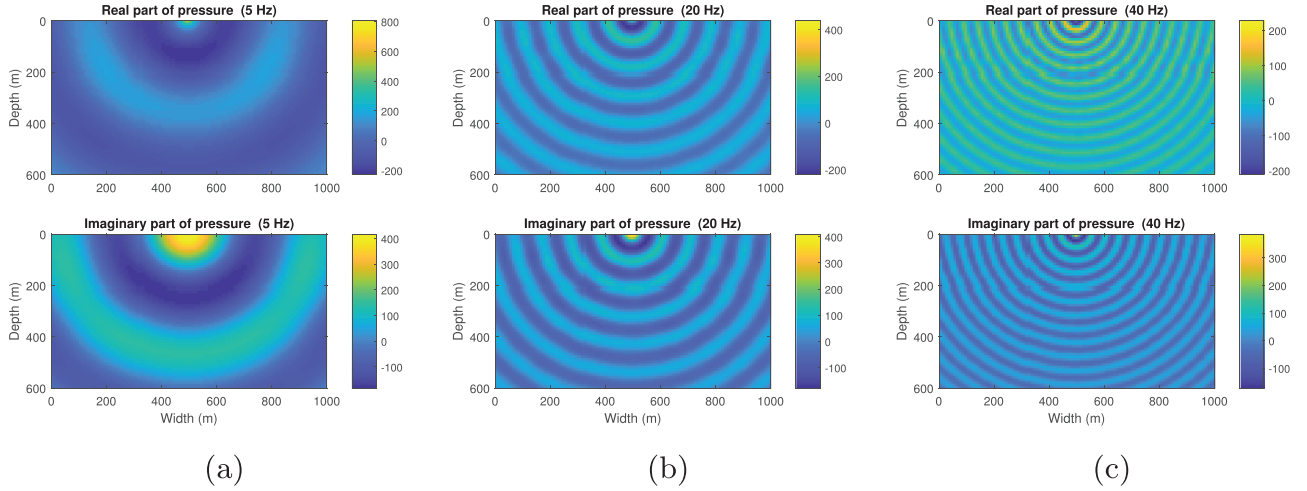
Figure 4 Reference wavefields at (a) 5 Hz, (b) 20 Hz and (c) 40 Hz via matrix inversion within the three-layer model in Figure 3
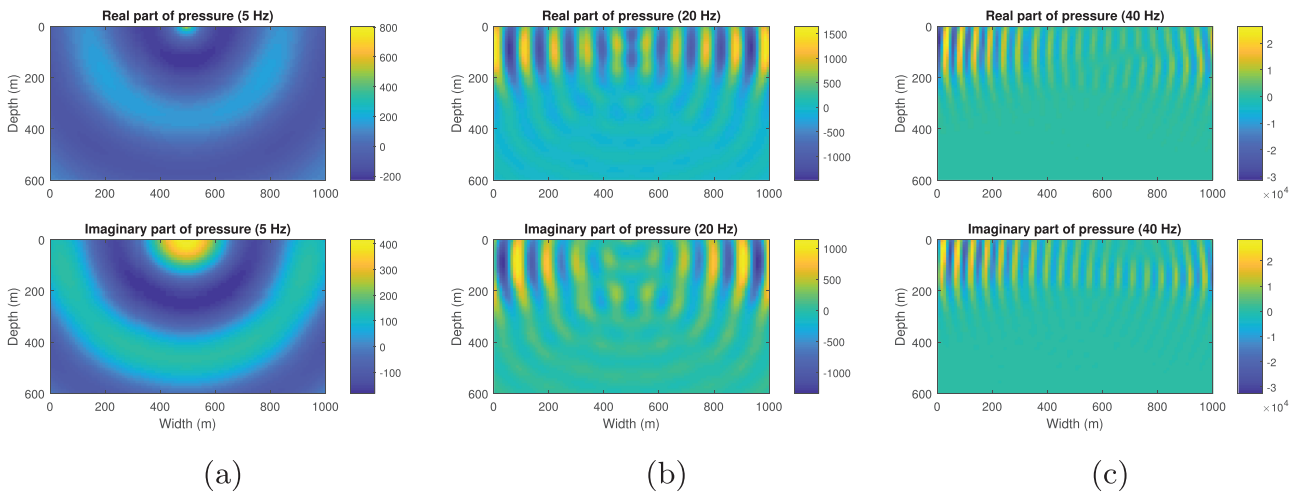

Figure 5 Wavefields at (a) 5 Hz, (b) 20 Hz and (c) 40 Hz via Born series within the three-layer model in Figure 3.

dependent on the angular frequency ω, but we will in the following suppress this dependency for simplicity.

We define the normalized contrasts in the mass density and bulk modulus fields by

$$\chi_\rho(\mathbf{x}) = \frac{\rho_0}{\rho(\mathbf{x})} - 1, \quad \chi_\kappa(\mathbf{x}) = \frac{\kappa_0}{\kappa(\mathbf{x})} - 1, \tag{2}$$

where ρ_0, $\kappa_0 = \rho_0 v_0^2$ and v_0 are the density, the bulk modulus and the velocity of a homogeneous background model. By combining (1) and (2), we obtain

$$\left(\frac{1}{\rho_0}\nabla^2 + \frac{\omega^2}{\kappa_0}\right)p(\mathbf{x}) = -S(\mathbf{x}) - \left[\nabla \cdot \frac{\chi_\rho(\mathbf{x})}{\rho_0}\nabla + \frac{\omega^2\chi_\kappa(\mathbf{x})}{\kappa_0}\right]p(\mathbf{x}). \tag{3}$$

We multiply both sides of (3) by ρ_0 and use $\kappa_0 = \rho_0 v_0^2$ to get

$$\left(\nabla^2 + k_0^2\right)p(\mathbf{x}) = -\rho_0 S(\mathbf{x}) - \left[\nabla \cdot \chi_\rho(\mathbf{x})\nabla + k_0^2\chi_\kappa(\mathbf{x})\right]p(\mathbf{x}), \tag{4}$$

where $k_0 = \omega/v_0$ is the wave number in the background medium.

The second term on the right-side of the equation (4) can be considered as secondary source. By using the volume integral (Morse and Feshbach, 1954), we represent the wavefield $p(\mathbf{x})$ as

$$p(\mathbf{x}) = p^{(0)}(\mathbf{x}) + \int d\mathbf{x}' g^{(0)}(\mathbf{x} - \mathbf{x}')\left[\nabla_{\mathbf{x}'} \cdot \chi_\rho(\mathbf{x}')\nabla_{\mathbf{x}'} + k_0^2\chi_\kappa(\mathbf{x}')\right]p(\mathbf{x}'), \tag{5}$$

where

$$p^{(0)}(\mathbf{x}) = \rho_0 \int d\mathbf{x}' g^{(0)}(\mathbf{x} - \mathbf{x}')S(\mathbf{x}') \tag{6}$$
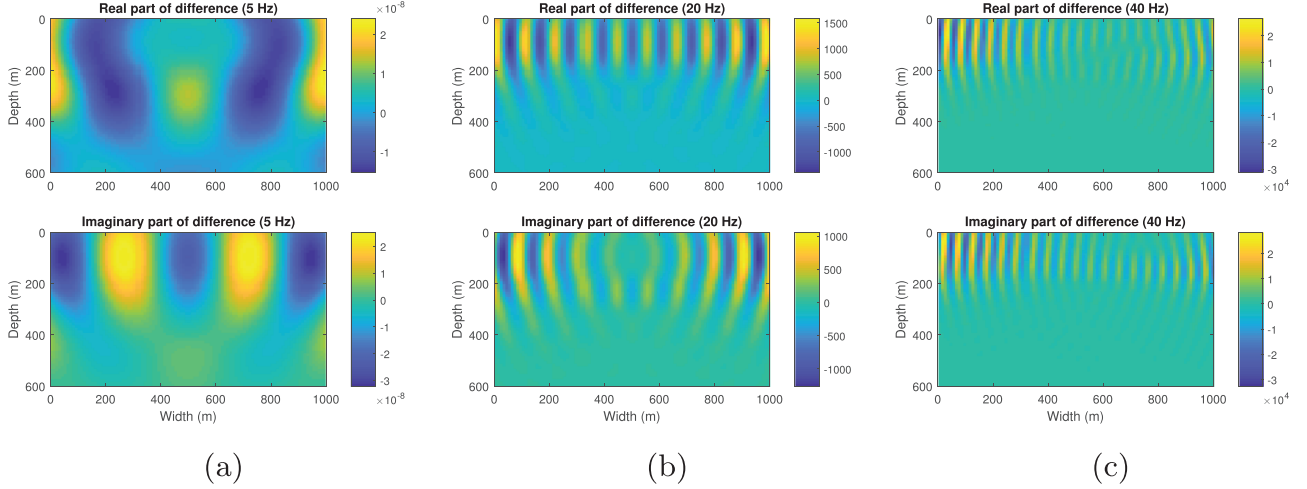
Figure 6 Differences between the Born-series wavefields and the reference wavefields at (a) 5 Hz, (b) 20 Hz and (c) 40 Hz within the three-layer model in Figure 3.
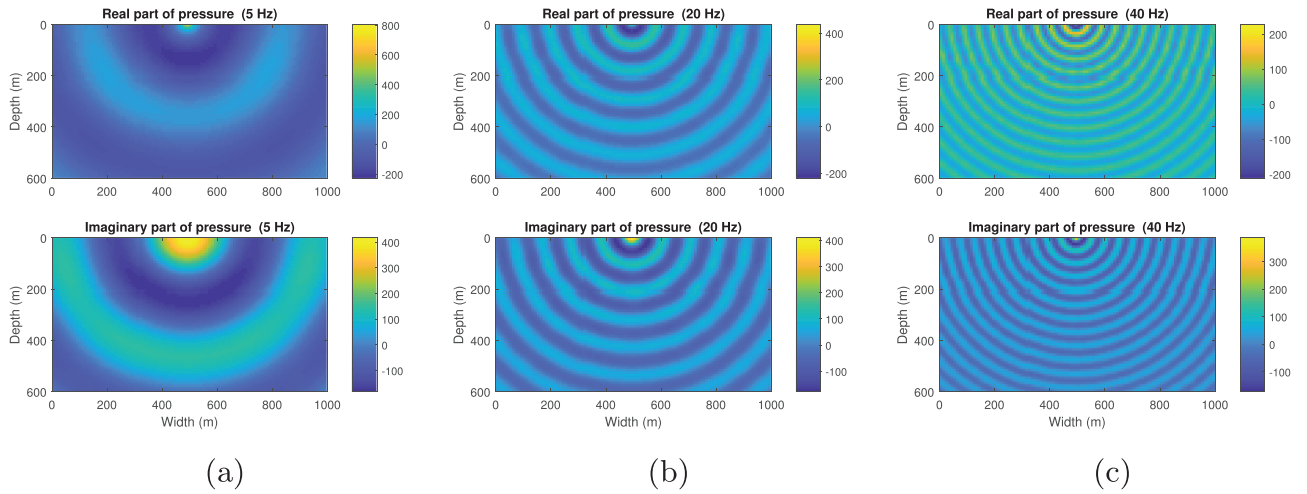

Figure 7 Wavefields at (a) 5 Hz, (b) 20 Hz and (c) 40 Hz via homotopy series within the three-layer model in Figure 3.

is the wavefield in the homogeneous background medium due to the actual source S and $g^{(0)}(\mathbf{x} - \mathbf{x}')$ is the Green's function for the homogeneous background medium that satisfies

$$\left(\nabla^2 + k_0^2\right)g^{(0)}(\mathbf{x} - \mathbf{x}') = -\delta(\mathbf{x} - \mathbf{x}'), \tag{7}$$

where $\delta(\mathbf{x} - \mathbf{x}')$ is the Dirac delta function and represents a point source. In this paper, we use the Green's function for the homogeneous acoustic medium (see Appendices A and B) to calculate $g^{(0)}(\mathbf{x} - \mathbf{x}')$. More details about the Green's function can be found in Arfken and Weber (1999).

The appearance of the divergence operator $\nabla_{\mathbf{x}'}$ on $\chi_\rho(\mathbf{x})$ makes the use of equation (5) complicated. By using the rule of divergence of a product (Arfken and Weber, 1999), we have

$$\int d\mathbf{x}' g^{(0)}(\mathbf{x} - \mathbf{x}')\nabla_{\mathbf{x}'} \cdot \left[\chi_\rho(\mathbf{x}')\nabla_{\mathbf{x}'}p(\mathbf{x}')\right]$$

$$= \int d\mathbf{x}' \nabla_{\mathbf{x}'} \cdot \left[g^{(0)}(\mathbf{x} - \mathbf{x}')\chi_\rho(\mathbf{x}')\nabla_{\mathbf{x}'}p(\mathbf{x}')\right]$$

$$- \int d\mathbf{x}' \nabla_{\mathbf{x}'}g^{(0)}(\mathbf{x} - \mathbf{x}') \cdot \chi_\rho(\mathbf{x}')\nabla_{\mathbf{x}'}p(\mathbf{x}'). \tag{8}$$

The first term on the right-hand side of (8) can be converted into a surface integral through Gauss's theorem, which goes
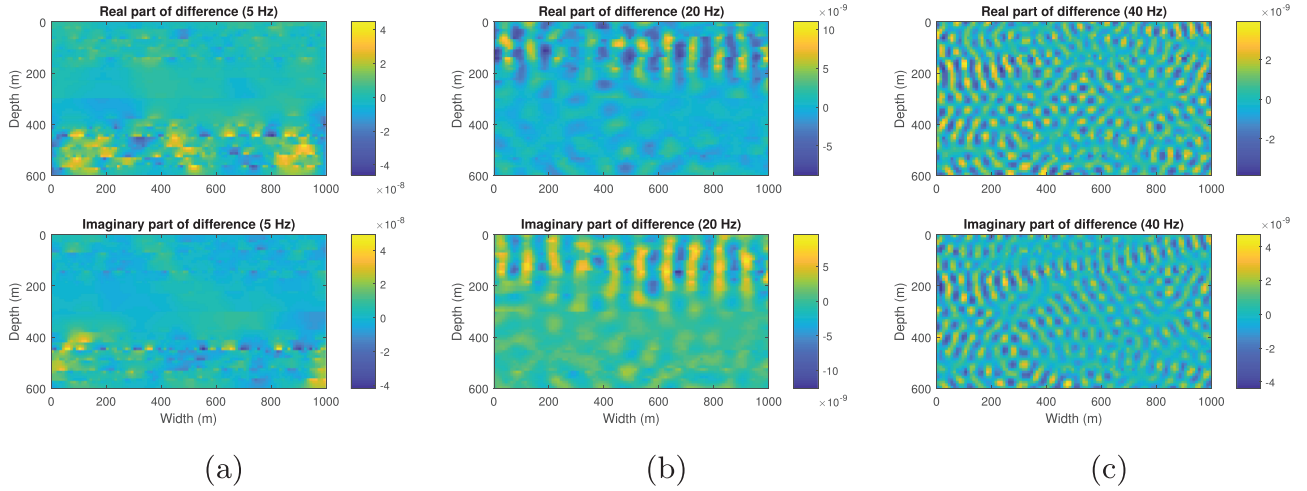
Figure 8 Differences between the homotopy-series wavefields and the reference wavefields at (a) 5 Hz, (b) 20 Hz and (c) 40 Hz within the three-layer model in Figure 3.
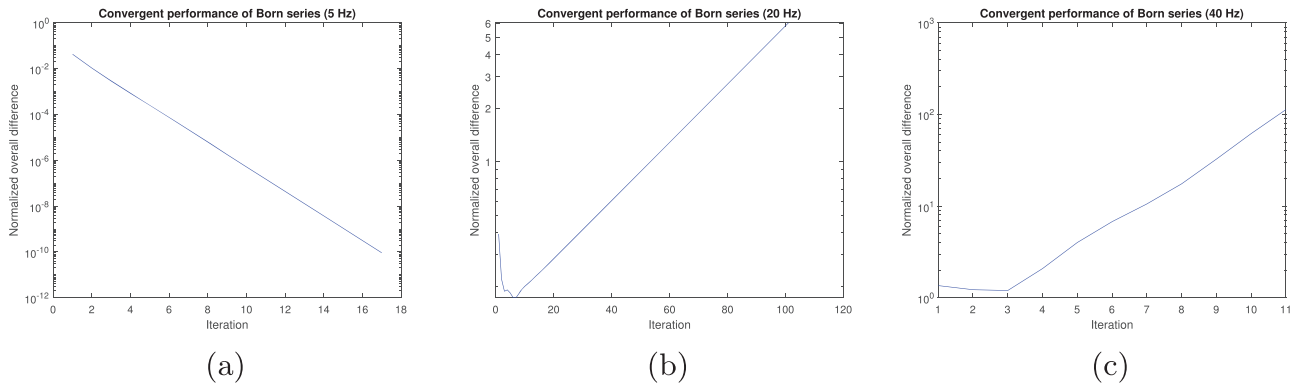

Figure 9 Normalized overall differences versus iteration for Born series at (a) 5 Hz, (b) 20 Hz and (c) 40 Hz within the three-layer model in Figure 3.

to zero because the Green's function and the fields approaches zero at infinity. By combining (5) and (8) and replacing $-\nabla_{\mathbf{x}'}$ with $\nabla_{\mathbf{x}}$, we obtain:

$$p(\mathbf{x}) = p^{(0)}(\mathbf{x}) + k_0^2 \int d\mathbf{x}' g^{(0)}(\mathbf{x} - \mathbf{x}') \chi_\kappa(\mathbf{x}') p(\mathbf{x}')$$
$$+ \int d\mathbf{x}' \nabla_{\mathbf{x}} g^{(0)}(\mathbf{x} - \mathbf{x}') \cdot \chi_\rho(\mathbf{x}') \nabla_{\mathbf{x}'} p(\mathbf{x}'). \tag{9}$$

In equation (9), there is no spatial derivative on $\chi_\rho(\mathbf{x}')$, which is useful for inversion. However, equation (9) also shows we need the spatial derivative of the pressure field to calculate the pressure field itself, which may be difficult for the forward

modelling. To mitigate this problem, we take spatial derivative on both sides of equation (9) and obtain

$$\nabla_{\mathbf{x}} p(\mathbf{x}) = \nabla_{\mathbf{x}} p^{(0)}(\mathbf{x}) + k_0^2 \int d\mathbf{x}' \nabla_{\mathbf{x}} g^{(0)}(\mathbf{x} - \mathbf{x}') \chi_\kappa(\mathbf{x}') p(\mathbf{x}')$$
$$+ \int d\mathbf{x}' \nabla_{\mathbf{x}} \nabla_{\mathbf{x}} g^{(0)}(\mathbf{x} - \mathbf{x}') \cdot \chi_\rho(\mathbf{x}') \nabla_{\mathbf{x}'} p(\mathbf{x}'). \tag{10}$$

Next we combine (9) and (10) into the vectorial Lippmann–Schwinger equation:

$$\boldsymbol{\psi}(\mathbf{x}) = \boldsymbol{\psi}^{(0)}(\mathbf{x}) + \int d\mathbf{x}' \mathbf{G}^{(0)}(\mathbf{x} - \mathbf{x}') \mathbf{V}(\mathbf{x}') \boldsymbol{\psi}(\mathbf{x}'), \tag{11}$$

where $\boldsymbol{\psi}(\mathbf{x}) = (p(\mathbf{x}), \nabla_{\mathbf{x}} p(\mathbf{x}))^\mathsf{T}$ and $\boldsymbol{\psi}^{(0)}(\mathbf{x}) = (p^{(0)}(\mathbf{x}), \nabla_{\mathbf{x}} p^{(0)}(\mathbf{x}))^\mathsf{T}$ is the combined wavefield, a $(n+1) \times 1$ vec-
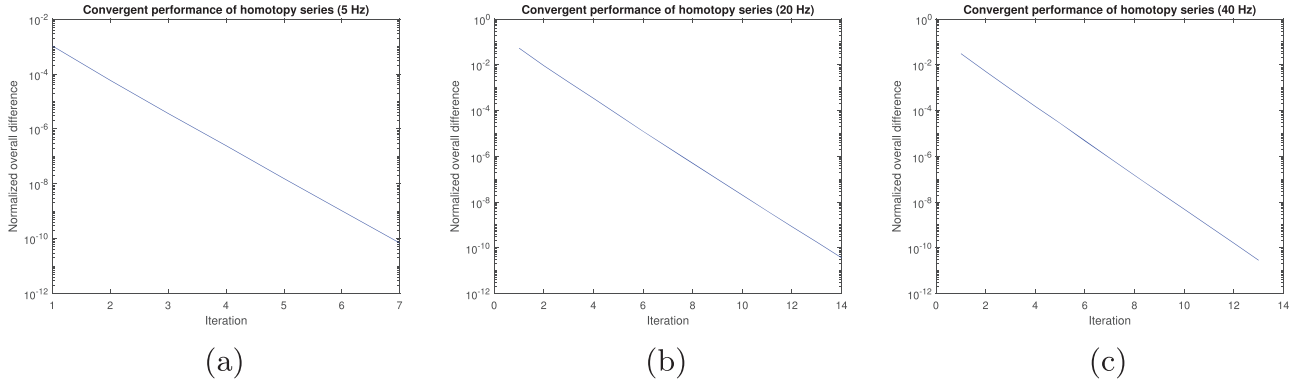
Figure 10 Normalized overall differences versus iteration for homotopy series at (a) 5 Hz, (b) 20 Hz and (c) 40 Hz within the three-layer model in Figure 3.
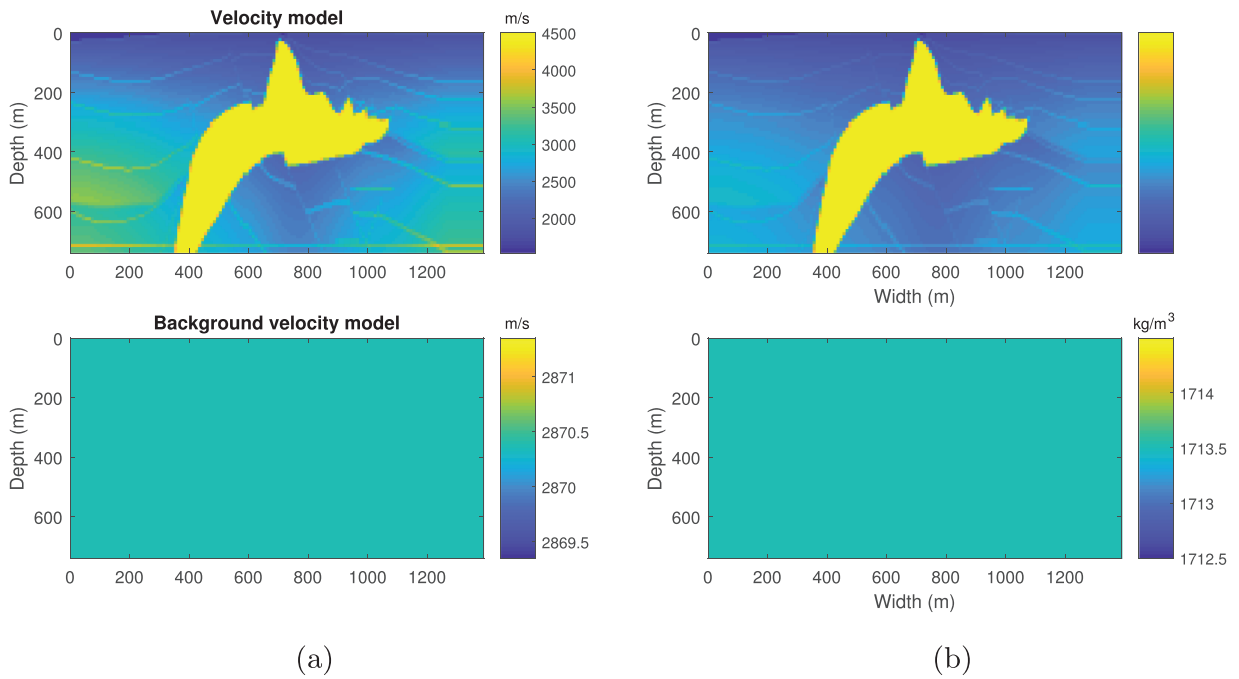

Figure 11 The resampled SEG/EAGE salt model and its background model.

tor, including the wavefield itself and its spatial derivative, in the actual and background medium, respectively;

$$
\mathbf{V}(\mathbf{x}') = \begin{pmatrix} \chi_\kappa(\mathbf{x}') & \mathbf{0}_n^{\mathsf{T}} \\ \mathbf{0}_n & \chi_\rho(\mathbf{x}')\mathbf{I}_n \end{pmatrix} \tag{12}
$$

is a $(n+1) \times (n+1)$ scattering potential operator including the contrast of bulk modulus and density, where $\mathbf{0}_n$ is an $n \times 1$ zero vector and $\mathbf{I}_n$ is an $n \times n$ identity matrix;

$$
\mathbf{G}^{(0)}(\mathbf{x} - \mathbf{x}') = \begin{pmatrix} k_0^2 g^{(0)}(\mathbf{x} - \mathbf{x}') & \left[\nabla_\mathbf{x} g^{(0)}(\mathbf{x} - \mathbf{x}')\right]^{\mathsf{T}} \\ k_0^2 \nabla_\mathbf{x} g^{(0)}(\mathbf{x} - \mathbf{x}') & \nabla_\mathbf{x} \nabla_\mathbf{x} g^{(0)}(\mathbf{x} - \mathbf{x}') \end{pmatrix} \tag{13}
$$

is an $(n+1) \times (n+1)$ operator including the Green's function and its first- and second-order spatial derivatives. More details about the Green's function and its first- and second-order spatial derivatives are given in Appendices A and B for the two-dimensional and three-dimensional cases, respectively.

Matrix representation of the vectorial LS equation

For the sake of simplicity, next we will present the matrix representation of the vectorial Lippmann–Schwinger (LS) equation in two-dimensional (2D) case. However, it can be
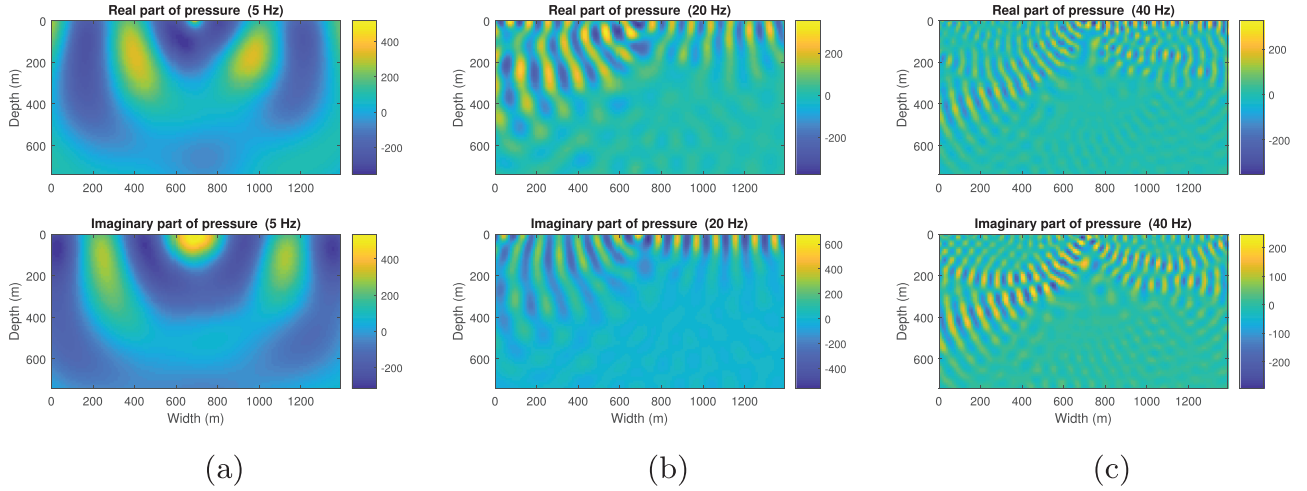
Figure 12 Reference wavefields at (a) 5 Hz, (b) 20 Hz and (c) 40 Hz via matrix inversion within the resampled SEG/EAGE salt model in Figure 11.
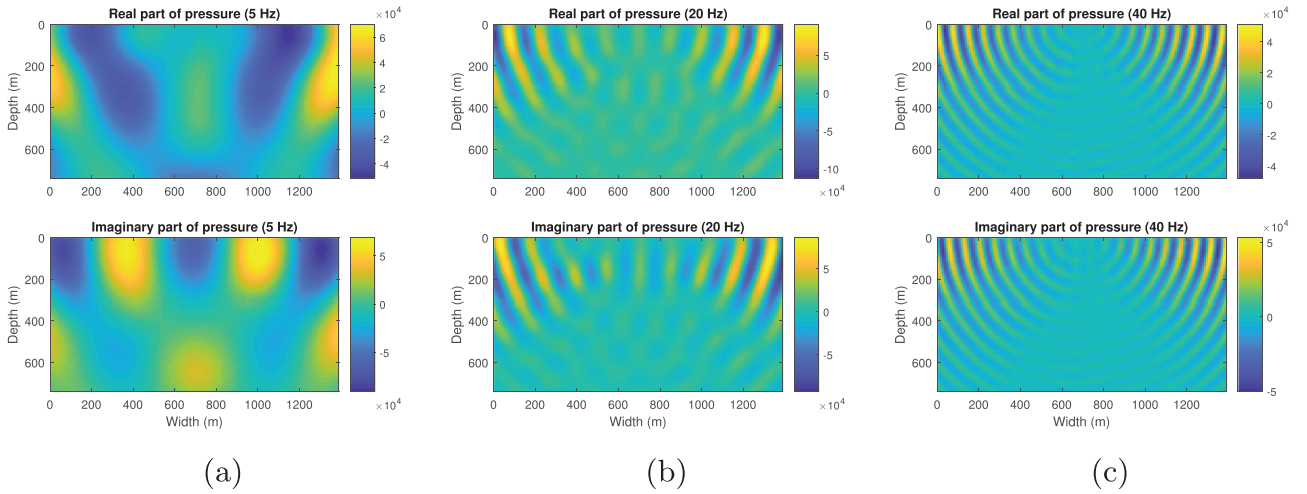

Figure 13 Wavefields at (a) 5 Hz, (b) 20 Hz and (c) 40 Hz via Born series within the resampled SEG/EAGE salt model in Figure 11.

extended to three-dimensional (3D) easily. We first divide the model into N grid blocks. At each grid block, the combined wavefield, presented by the combined wavefield at the centroid of that grid block, includes the wavefield p and its spatial derivative ∇p. In 2D case, ∇p has two components ∇p_1 and ∇p_2; ∇g has two components ∇g_1 and ∇g_2 and $\nabla\nabla g$ has four components $\nabla\nabla g_{11}$, $\nabla\nabla g_{12}$, $\nabla\nabla g_{21}$ and $\nabla\nabla g_{22}$. Next we formulate the combined wavefield at all points of the discrete domain and rearrange them into vectors $\psi = (\mathbf{p}, \nabla\mathbf{p}_1, \nabla\mathbf{p}_2)^\mathsf{T}$, where $\mathbf{p} = (p_1, \ldots, p_N)^\mathsf{T}$, $\nabla\mathbf{p}_1 = (\nabla p_1^1, \ldots, \nabla p_1^N)^\mathsf{T}$ and $\nabla\mathbf{p}_2 = (\nabla p_2^1, \ldots, \nabla p_2^N)^\mathsf{T}$. Finally we obtain the matrix representation of the vectorial LS equation:

$$\psi = \psi^{(0)} + \mathbf{G}^{(0)}\mathbf{V}\psi, \tag{14}$$

where

$$\psi^{(0)} = (\mathbf{p}^{(0)}, \nabla\mathbf{p}_1^{(0)}, \nabla\mathbf{p}_2^{(0)})^\mathsf{T}; \tag{15}$$

$$\mathbf{V} = \begin{pmatrix} \chi_\kappa & \mathbf{0} & \mathbf{0} \\ \mathbf{0} & \chi_\rho & \mathbf{0} \\ \mathbf{0} & \mathbf{0} & \chi_\rho \end{pmatrix}; \tag{16}$$

$$\mathbf{G}^{(0)} = \begin{pmatrix} k_0^2\mathbf{g}^{(0)} & \nabla\mathbf{g}_1^{(0)} & \nabla\mathbf{g}_2^{(0)} \\ k_0^2\nabla\mathbf{g}_1^{(0)} & \nabla\nabla\mathbf{g}_{11}^{(0)} & \nabla\nabla\mathbf{g}_{12}^{(0)} \\ k_0^2\nabla\mathbf{g}_2^{(0)} & \nabla\nabla\mathbf{g}_{21}^{(0)} & \nabla\nabla\mathbf{g}_{22}^{(0)} \end{pmatrix}. \tag{17}$$

In equation (16), χ_κ and χ_ρ are both an $N \times N$ diagonal matrix and $\mathbf{0}$ is a $N \times N$ zero matrix. In equation (17), all blocks of $\mathbf{G}^{(0)}$ are $N \times N$ matrix.
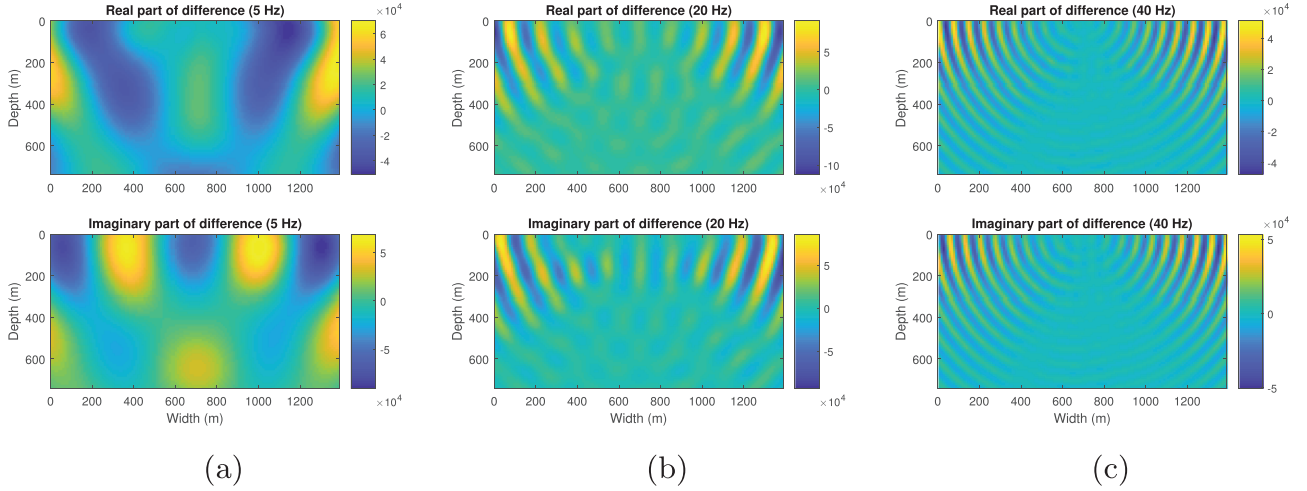
Figure 14 Differences between the Born-series wavefields and the reference wavefields at (a) 5 Hz, (b) 20 Hz and (c) 40 Hz within the resampled SEG/EAGE salt model in Figure 11.
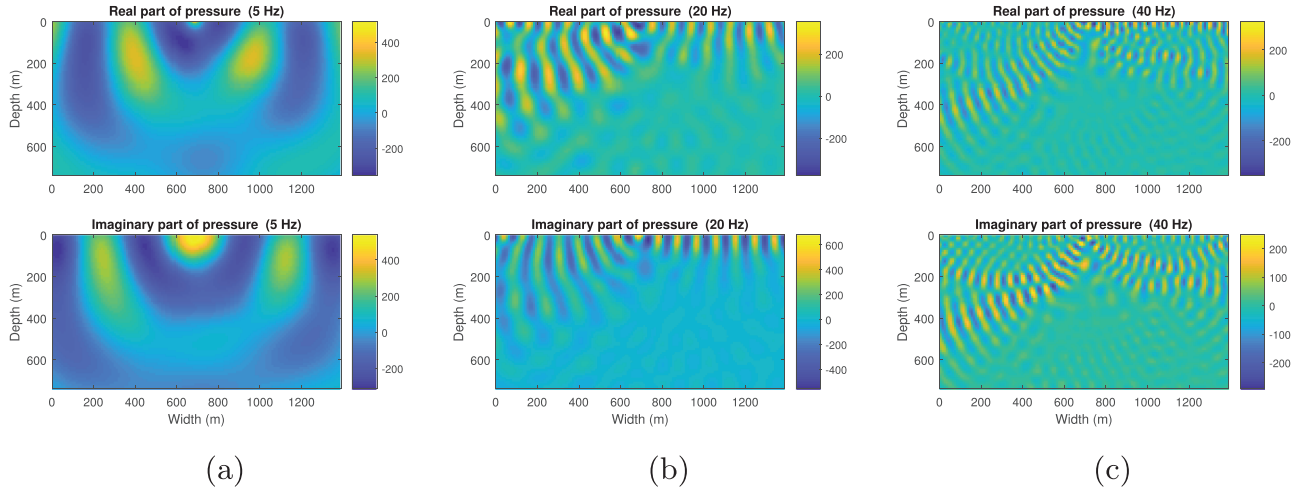

Figure 15 Wavefields at (a) 5 Hz, (b) 20 Hz and (c) 40 Hz via homotopy series within the resampled SEG/EAGE salt model in Figure 11.

The wavefield ψ in equation (14) can be solved through matrix inversion:

$$\psi = (\mathbf{I} - \mathbf{G}^{(0)}\mathbf{V})^{-1}\psi^{(0)}, \tag{18}$$

where $\mathbf{I}$ is a $3N \times 3N$ identity matrix. However, the computational cost of inverting a huge full matrix $\mathbf{I} - \mathbf{G}^{(0)}\mathbf{V}$ scales like N^3, which is costly due to the large number of grid blocks in practical applications.

The Born series iteration

As mentioned above, solving equation (18) is costly in the realistic case. In order to solve the problem of high-computational

cost, we use iterative methods, instead of matrix inversion, to solve equation (14). One of the most well-known iterative methods is the Born series solution (Morse and Feshbach, 1954):

$$\psi = (\mathbf{I} + \mathbf{G}^{(0)}\mathbf{V} + \mathbf{G}^{(0)}\mathbf{V}\mathbf{G}^{(0)}\mathbf{V} + \cdots)\psi^{(0)}. \tag{19}$$

Equation (19) can be rewritten in iterative form as

$$\psi^k = \psi^{(0)} + \mathbf{G}^{(0)}\mathbf{V}\psi^{k-1}, \quad k \geq 1, \tag{20}$$

where ψ^k is an estimate of the total wavefield after k iterations, which is equal to the partial sum of the first k terms in (19). When $\| \psi^k - \psi^{k-1} \|$ is small, the iterations are stopped, and the computational cost of (20) scales as N^2. The cost is
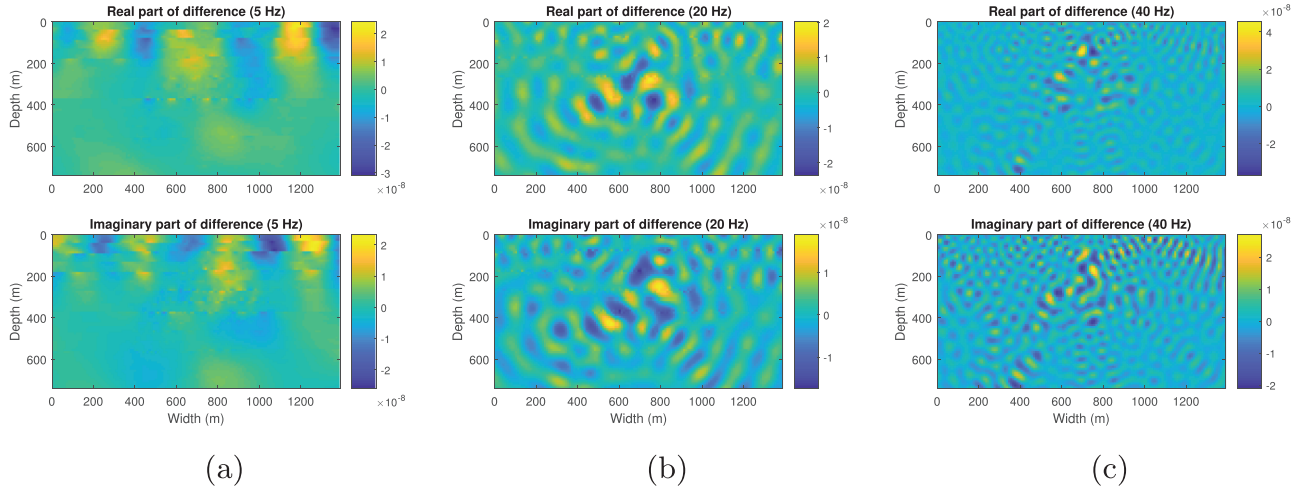
Figure 16 Differences between the homotopy-series wavefields and the reference wavefields at (a) 5 Hz, (b) 20 Hz and (c) 40 Hz within the resampled SEG/EAGE salt model in Figure 11.
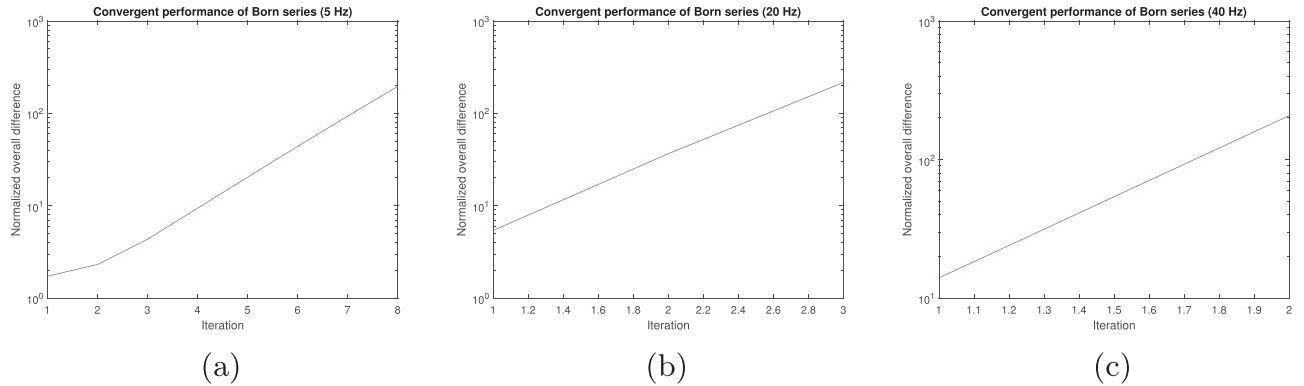

Figure 17 Normalized overall differences versus iteration for Born series at (a) 5 Hz, (b) 20 Hz and (c) 40 Hz within the resampled SEG/EAGE salt model in Figure 11.

greatly reduced compared with matrix inversion (18). However, the Born series iteration is only guaranteed to converge when the spectral radius, $\sigma(\mathbf{G}^{(0)}\mathbf{V})$, is smaller than unity, which means that the Born series iteration is only suitable for weak scattering contrast and low-frequency situations (Innanen, 2009; Wu and Zheng, 2014; Osnabrugge *et al.*, 2016; Huang *et al.*, 2020). In the next section, we will describe an approach that still converges when the Born series iteration diverges.

Homotopy analysis method for the vectorial LS equation

In order to find an iterative method that converges even in strongly scattering media and for high frequencies, we introduce the homotopy analysis method to solve equation (14).

The main idea of the homotopy analysis method is to introduce an embedding parameter to the solution of linear or non-linear problems and let the solution change from the initial value to the final solution as the embedding parameter changes. We first introduce the zero-order deformation equation of equation (14) (Liao, 1997, 2003; Liao and Tan, 2007; Huang and Greenhalgh, 2018; Jakobsen *et al.*, 2020):

$$(1 - \lambda)[\boldsymbol{\psi}(\lambda) - \boldsymbol{\psi}_0] = -\lambda\mathbf{H}[\boldsymbol{\psi}(\lambda) - \boldsymbol{\psi}^{(0)} - \mathbf{G}^{(0)}\mathbf{V}\boldsymbol{\psi}(\lambda)], \quad (21)$$

where $\lambda \in [0, 1]$ is the embedding parameter, $\mathbf{H}$ is the convergence control operator and $\boldsymbol{\psi}(\lambda)$ is the solution related to the embedding parameter. In equation (21), we see that when $\lambda = 0$, $\boldsymbol{\psi}(0) = \boldsymbol{\psi}_0$, which means $\boldsymbol{\psi}(0)$ is the initial solution; and when $\lambda = 1$, then $\boldsymbol{\psi}(1) = \boldsymbol{\psi}^{(0)} + \mathbf{G}^{(0)}\mathbf{V}\boldsymbol{\psi}(1)$, which means that $\boldsymbol{\psi}(1) = \boldsymbol{\psi}$ is the solution of equation (14). The above
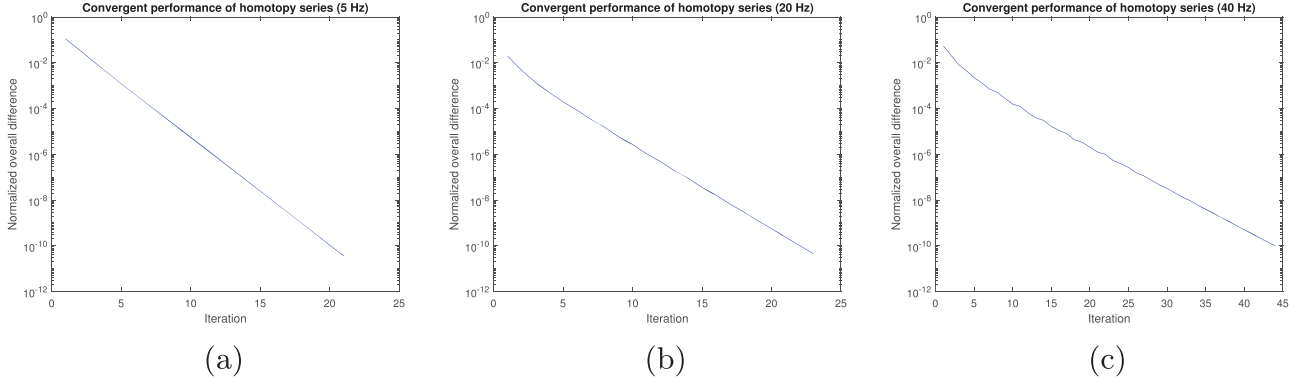
Figure 18 Normalized overall differences versus iteration for homotopy series at (a) 5 Hz, (b) 20 Hz and (c) 40 Hz within the resampled SEG/EAGE salt model in Figure 11.

analysis shows that if we gradually change λ from 0 to 1, we get the final solution of equation (14) from the initial solution. Based on the above analysis, we expand the unknown solution $\boldsymbol{\psi}(\lambda)$ in a Maclaurin series:

$$\boldsymbol{\psi}(\lambda) = \boldsymbol{\psi}(0) + \boldsymbol{\psi}'(0)\lambda + \frac{\boldsymbol{\psi}''(0)}{2!}\lambda^2 + \cdots + \frac{\boldsymbol{\psi}^{(m)}(0)}{m!}\lambda^m + \cdots \tag{22}$$

$$= \boldsymbol{\psi}_0 + \boldsymbol{\psi}_1\lambda + \boldsymbol{\psi}_2\lambda^2 + \cdots + \boldsymbol{\psi}_m\lambda^m + \cdots .$$

To make further progress, we assume that the convergence control operator $\mathbf{H}$ can be selected such that the Maclaurin series (22) is convergent at $\lambda = 1$. So the final solution of equation (14) can be expressed as (Liao, 2003)

$$\boldsymbol{\psi} = \boldsymbol{\psi}_0 + \boldsymbol{\psi}_1 + \boldsymbol{\psi}_2 + \cdots + \boldsymbol{\psi}_m + \cdots . \tag{23}$$

By taking the derivation of both sides of (21) m times with respect to λ, dividing the derivation result by $m!$ and setting λ equal to 0, we find that $\boldsymbol{\psi}_{m-1}$ and $\boldsymbol{\psi}_m$ in (23) have this relationship (Jakobsen *et al.*, 2020):

$$\boldsymbol{\psi}_m = \mathbf{M}\boldsymbol{\psi}_{m-1}, \quad m \geq 2, \tag{24}$$

where

$$\mathbf{M} = \mathbf{I} - \mathbf{H} + \mathbf{H}\mathbf{G}^{(0)}\mathbf{V}, \tag{25}$$

$$\boldsymbol{\psi}_1 = \mathbf{H}(\boldsymbol{\psi}^{(0)} - \boldsymbol{\psi}_0 + \mathbf{G}^{(0)}\mathbf{V}\boldsymbol{\psi}_0). \tag{26}$$

By combining (23)–(26), we finally obtain the homotopy analysis scattering series

$$\boldsymbol{\psi} = \boldsymbol{\psi}_0 + (\mathbf{I} + \mathbf{M} + \mathbf{M}^2 + \cdots)\boldsymbol{\psi}_1, \tag{27}$$

where $\boldsymbol{\psi}_0$ can be selected as $\boldsymbol{\psi}^{(0)}, \mathbf{H}\boldsymbol{\psi}^{(0)}$ or other initial guess. If the spectral radius of $\mathbf{M}$ satisfies $\sigma(\mathbf{M}) < 1$, the homotopy series (27) will converge, which means the series (23) converges and the Maclaurin series (22) is convergent at $\lambda = 1$. From

equation (25), we find it is possible to choose an appropriate $\mathbf{H}$ to ensure $\sigma(\mathbf{M}) < 1$ so that all above series are convergent.

Equation (27) can be rewritten in the iterative form as

$$\boldsymbol{\psi}^k = -\mathbf{M}\boldsymbol{\psi}_0 + \boldsymbol{\psi}^2 + \mathbf{M}\boldsymbol{\psi}^{k-1}, \quad k \geq 3, \tag{28}$$

where

$$\boldsymbol{\psi}^1 = \mathbf{H}(\boldsymbol{\psi}^{(0)} - \boldsymbol{\psi}_0 + \mathbf{G}^{(0)}\mathbf{V}\boldsymbol{\psi}_0), \tag{29}$$

$$\boldsymbol{\psi}^2 = \boldsymbol{\psi}_0 + \boldsymbol{\psi}^1. \tag{30}$$

The main difference between the Born series (19) and the homotopy series (27) is the introduction of the convergence control operator $\mathbf{H}$, which makes the homotopy scattering series more flexible in convergence than the conventional Born series.

The construction of H by hierarchical matrices

In order to find a suitable $\mathbf{H}$, we adopt the method based on matrix low-rank approximation and hierarchical matrix proposed by Eikrem *et al.* (2020). The key idea of this method is to find an $\mathbf{H}$ to make the spectral radius $\sigma(\mathbf{M})$ as close to 0 as possible, so as to ensure that the homotopy scattering series converges. When we set $\mathbf{M} = 0$ in equation (25), we obtain $\mathbf{H} = (\mathbf{I} - \mathbf{G}^{(0)}\mathbf{V})^{-1}$. It can be seen that if $\mathbf{H}$ approximates $(\mathbf{I} - \mathbf{G}^{(0)}\mathbf{V})^{-1}$, then $\mathbf{M} \approx 0$ and $\sigma(\mathbf{M}) \approx 0$. Next we will use the hierarchical matrices to approximate $\mathbf{I} - \mathbf{G}^{(0)}\mathbf{V}$ and find the approximation of its inverse.

A hierarchical matrix is an approximation of a full matrix that is constructed by dividing this full matrix into blocks based on a cluster tree structure (Börm *et al.*, 2003). As shown in Figure 1, we first partition the matrix into four parts. Next, we use the low-rank approximation algorithm of a matrix

Table 2 Computational time of different methods

Frequency	The three-layer model			The resampled SEG/EAGE salt model		
	5 Hz	20 Hz	40 Hz	5 Hz	20 Hz	40 Hz
Matrix inversion	111 s	117 s	111 s	589 s	675 s	606 s
Born series	8 s	diverge	diverge	diverge	diverge	diverge
Homotopy series	23 s	30 s	43 s	77 s	145 s	227 s

(Algorithm 1 in Eikrem *et al.* (2020), see also Halko *et al.* (2011)) to represent the non-diagonal blocks (the white blocks) as

$$\mathbf{E} = \mathbf{U}\mathbf{W}^{\mathsf{T}}, \tag{31}$$

where $\mathbf{E}$ is $N \times N$ matrix, $\mathbf{U}$ and $\mathbf{W}$ are $N \times r$ matrices and r is the rank much smaller than N. After that we further divide the diagonal blocks (the grey blocks) into four new blocks and repeat the above steps for the diagonal blocks. We call the left, middle and right hierarchical matrices in Figure 1 1, 2 and 3 level hierarchical matrices according to the number of divisions. Through further division, we also get higher level hierarchical matrices.

By using equations (16) and (17), we have

$$\mathbf{I} - \mathbf{G}^{(0)}\mathbf{V} = \begin{pmatrix} \mathbf{I}_N - k_0^2 \mathbf{g}^{(0)} \mathbf{\chi}_\kappa & -\nabla \mathbf{g}_1^{(0)} \mathbf{\chi}_\rho & -\nabla \mathbf{g}_2^{(0)} \mathbf{\chi}_\rho \\ -k_0^2 \nabla \mathbf{g}_1^{(0)} \mathbf{\chi}_\kappa & \mathbf{I}_N - \nabla \nabla \mathbf{g}_{11}^{(0)} \mathbf{\chi}_\rho & -\nabla \nabla \mathbf{g}_{12}^{(0)} \mathbf{\chi}_\rho \\ -k_0^2 \nabla \mathbf{g}_2^{(0)} \mathbf{\chi}_\kappa & -\nabla \nabla \mathbf{g}_{21}^{(0)} \mathbf{\chi}_\rho & \mathbf{I}_N - \nabla \nabla \mathbf{g}_{22}^{(0)} \mathbf{\chi}_\rho \end{pmatrix}, \tag{32}$$

where $\mathbf{I}_N$ is an $N \times N$ identity matrix. According to the value of each block of the right-hand side of (32), we re-divide $\mathbf{I} - \mathbf{G}^{(0)}\mathbf{V}$ into sub-matrices as shown in Figure 2 (middle). Next we construct the hierarchical matrix for each block of Figure 2 (middle) and combine $\mathbf{B}_1, \mathbf{B}_2$ and $\mathbf{C}_1, \mathbf{C}_2$ into one block $\mathbf{B}$ and $\mathbf{C}$. Now we have the hierarchical $\mathbf{I} - \mathbf{G}^{(0)}\mathbf{V}$ (Fig. 2 (right)).After getting the hierarchical matrix, we use the 2×2 block matrix inversion recursively to find its inverse:

$$\begin{pmatrix} \mathbf{A} & \mathbf{B} \\ \mathbf{C} & \mathbf{D} \end{pmatrix}^{-1} = \begin{pmatrix} \mathbf{A}^{-1} + \mathbf{A}^{-1}\mathbf{B}(\mathbf{D} - \mathbf{C}\mathbf{A}^{-1}\mathbf{B})^{-1}\mathbf{C}\mathbf{A}^{-1} & -\mathbf{A}^{-1}\mathbf{B}(\mathbf{D} - \mathbf{C}\mathbf{A}^{-1}\mathbf{B})^{-1} \\ -(\mathbf{D} - \mathbf{C}\mathbf{A}^{-1}\mathbf{B})^{-1}\mathbf{C}\mathbf{A}^{-1} & (\mathbf{D} - \mathbf{C}\mathbf{A}^{-1}\mathbf{B})^{-1} \end{pmatrix}. \tag{33}$$

The inverse of hierarchical $\mathbf{I} - \mathbf{G}^{(0)}\mathbf{V}$ is the $\mathbf{H}$ we are looking for. In Figure 1, only the grey blocks need to be fully inverted, which means that we use a series of small matrix inversions to approximate the inversion of a huge matrix. A more detailed description about hierarchical matrices can be found in Eikrem *et al.* (2020).

NUMERICAL EXAMPLES

In order to test the validity of our method, we use the homotopy series and Born series to calculate the wavefields in a three-layer model and a resampled SEG/EAGE salt model (Aminzadeh *et al.*, 1997) with different frequencies. The wavefield in acoustic media is pressure. To quantify the difference between the reference wavefield computed via matrix inversion and the iterative methods, we compute the normalized overall difference ϵ which is defined as

$$\epsilon_k = \| \mathbf{\psi}^k - \mathbf{\psi}^{(r)} \| / \| \mathbf{\psi}^{(r)} \|, \tag{34}$$

where $\mathbf{\psi}^{(r)}$ is the reference wavefield computed from equation (18) and $\mathbf{\psi}^k$ is the iterative wavefield after kth iteration. We use a homogeneous background medium with velocity and density equal to the averages of the actual model. We use a pulse with an amplitude of 1 to simulate a source term located exactly in the middle of the upper row of the model. We set $\mathbf{\psi}_0 = \mathbf{\psi}^{(0)}$ in the Born series and $\mathbf{\psi}_0 = \mathbf{H}\mathbf{\psi}^{(0)}$ in the homotopy series. We use different levels and ranks for the hierarchical matrix construction of different blocks in Figure 2 (middle). Because the values in $\mathbf{A}, \mathbf{B}_1, \mathbf{B}_2$ is higher than that in $\mathbf{C}_1, \mathbf{C}_2, \mathbf{D}$, we set a higher rank (called rank1 in Table 1) for $\mathbf{A}, \mathbf{B}_1, \mathbf{B}_2$ and a lower rank (called rank2 in Table 1) for $\mathbf{C}_1, \mathbf{C}_2, \mathbf{D}$. Table 1 shows all the levels and ranks we used to construct the hierarchical matrices for different models and frequencies.

First we calculate wavefields in the three-layer model (Fig. 3). The size of this model is 1000 m wide and 600 m deep. The discrete grid size of the real-space in horizontal and vertical direction are both 10 m. Ideally the space grid should go to 0, but that is not necessary. So usually we choose the grid spacing interval smaller than 1/4 of the smallest wavelength $\lambda_{\min}$, which means the grid spacing interval should smaller than $v_{\min}/4 f_{\max}$. The number of grid blocks is $N = 100 \times 60 = 6000$. Figure 4 shows reference wavefields of different frequencies calculated by matrix inversion (18). Figure 5 shows the real and imaginary part of wavefields at different frequencies obtained from the Born series. Figure 6 shows the differences between Born-series wavefields and reference

wavefields at different frequencies. Figure 7 shows wavefields at different frequencies obtained from the homotopy series. Figure 8 shows the differences between homotopy-series wavefields and reference wavefields at different frequencies. We also computed the normalized overall difference to quantify the convergence performance of the Born series and homotopy series. Figure 9 shows the normalized overall difference changes with iterations for the Born series. Figure 10 shows the normalized overall difference as a function of iteration for the homotopy series. From Figures 4–10, we can see:

1. The wavefields from the homotopy series matches well with the reference wavefields at all frequencies;

2. The Born series only converges at very low frequencies;

3. The homotopy series still converges when the Born series diverges;

Next we calculate the wavefield in the resampled SEG/EAGE salt model (Fig. 11). The density of this model (Fig. 11b, upper) apart from the salt dome portion is obtained from velocity (Fig. 11a, upper) by Gardner's relation: $\rho = 230v^{0.25}$ (Gardner *et al.*, 1974). The density of the salt dome portion is set equal to the density of halite, which is 2160 kg/m^3 (Mavko *et al.*, 2009). The size of this model is 1390 m wide and 740 m deep. The grid size of each discrete point is 10 m × 10 m. The number of grid blocks is $N = 139 \times 74 = 10,286$. Figure 12 shows the reference wavefield obtained via matrix inversion at different frequencies. Figures 13 and 15 show the wavefield at different frequencies via the Born series and the homotopy series. Figure 14 and 16 show the differences for Born and homotopy series at different frequencies. Figures 17 and 18 present the convergence performance of the Born series and the homotopy series. Clearly, we see that the wavefield from homotopy series is similar to the reference wavefield and the normalized overall difference becomes very small after up to 45 iterations while the wavefield produced using the Born series is totally different from the reference wavefield, and the normalized overall difference diverges in all frequencies.

Table 2 shows the computational time of different method for different models and frequencies. From Table 2, we see: (1) Matrix inversion is the most time-consuming method; (2) In the case of convergence, Born series is the least time-consuming; (3) Born series only converges at low frequencies in low contrast model; That is because even if the contrast of density or the bulk modulus is very small, putting them together will make the entire contrast arise; (4) Homotopy series not only guarantees convergence in all cases, it also takes much less time than matrix inversion; (5) The larger the model, the more time homotopy series saves compared to ma-

trix inversion. All experiments are performed on an computer with an Intel i7-7700, a 3.6 GHz CPU and a 64 GB RAM.

CONCLUSIONS

We have derived a vectorial integral equation of the Lippmann-Schwinger (LS) type for seismic forward modelling in acoustic medium with variable velocity and density. This vectorial LS equation is derived from two coupled integral equations. In order to solve it efficiently, we have introduced the homotopy analysis method. The homotopy series is obtained after solving the vectorial LS equation with the homotopy analysis method. It is more flexible than the conventional Born series due to the introduction of the convergence control operator $\mathbf{H}$. We have analysed that if $\mathbf{H}$ approximates $(\mathbf{I} - \mathbf{G}^{(0)}\mathbf{V})^{-1}$, the homotopy series will converge. Based on this, we constructed the convergence control operator $\mathbf{H}$ by using low-rank matrix approximation and hierarchical matrices.

On the basis of the numerical experiments, we have compared the performance of homotopy series with conventional Born series and matrix inversion. Compared with the conventional Born series, the corresponding homotopy series assures convergence in high contrast media and for high frequencies. Compared with matrix inversion, the homotopy series reduces the scale of computational cost from N^3 to N^2, where N is the number of grid blocks. Numerical examples also show that the larger the model, the more computational time is reduced. This makes our approach suitable for the application of realistic large problems.

This paper mainly focuses on providing a new perspective for seismic forward modelling with variable density and velocity. In future work, an investigation of the optimal form of the hierarchical matrices for constructing convergence control operators as well as the use of Fast Fourier Transform in the construction of the hierarchical matrices (Eikrem *et al.*, 2020) should be included. Also, it might be interesting to use the vectorial LS equation and its homotopy series solution for simultaneous inversion of velocity and density.

DATA AVAILABILITY STATEMENT

The data that support this study are available from the corresponding author on reasonable request.

ORCID

Kui Xiang 🆔 https://orcid.org/0000-0002-4683-919X
Morten Jakobsen 🆔 https://orcid.org/0000-0001-8861-1938

REFERENCES

Abhishek, A., Bonnet, M. & Moskow, S. (2020) Modified forward and inverse Born series for the Calderon and diffuse-wave problems. *Inverse Problems*, 36(11), 114001.

Abubakar, A., Van Den Berg, P. & Fokkema, J. (2003) Towards non-linear inversion for characterization of time-lapse phenomena through numerical modelling. *Geophysical Prospecting*, 51(4), 285–293.

Aki, K. & Richards, P. G. (1980) *Quantitative Seismology: Theory and Methods*. New York, NY: W. H. Freeman and Company.

Allgower, E. & Georg, K. (1990) *Numerical Continuation Methods - An Introduction*. Berlin–Heidelberg: Springer.

Aminzadeh, F., Brac, J. & Kunz, T. (1997) *3-D Salt and Overthrust Models*. Tulsa, OK: Society of Exploration Geophysicists.

Arfken, G. B. & Weber, H. J. (1999) *Mathematical Methods for Physicists*. College Park, MD: American Association of Physics Teachers.

Bonnet, M. (2017) A modified volume integral equation for anisotropic elastic or conducting inhomogeneities: unconditional solvability by Neumann series. *Journal of Integral Equations and Applications*, 29(2), 271–295.

Börm, S., Grasedyck, L. & Hackbusch, W. (2003) Introduction to hierarchical matrices with applications. *Engineering Analysis With Boundary Elements*, 27, 405–422.

Carcione, J. M., Herman, G. C. & Ten Kroode, A. (2002) Seismic modeling. *Geophysics*, 67(4), 1304–1325.

Eftekhar, R., Hu, H. & Zheng, Y. (2018) Convergence acceleration in scattering series and seismic waveform inversion using nonlinear shanks transformation. *Geophysical Journal International*, 214(3), 1732–1743.

Eikrem, K. S., Nævdal, G. & Jakobsen, M. (2020) Iterative solution of the Lippmann-Schwinger equation in strongly scattering acoustic media by randomized construction of preconditioners. *Geophysical Journal International*, 224(3), 2121–2130.

Farshad, M. & Chauris, H. (2020) From constant to variable density inverse extended Born modeling. *Geophysics*, 85(4), S217–S232.

Gardner, G., Gardner, L. & Gregory, A. (1974) Formation velocity and density': the diagnostic basics for stratigraphic traps. *Geophysics*, 39(6), 770–780.

Halko, N., Martinsson, P.-G. & Tropp, J. A. (2011) Finding structure with randomness: probabilistic algorithms for constructing approximate matrix decompositions. *SIAM Review*, 53(2), 217–288.

Hanyga, A. & Pajchel, J. (1995) Point-to-curve ray tracing in complicated geological models. *Geophysical Prospecting*, 43(7), 859–872.

Huang, X. & Greenhalgh, S. (2018) Traveltime approximation for strongly anisotropic media using the homotopy analysis method. *Geophysical Journal International*, 216(3), 1648–1664.

Huang, X., Jakobsen, M., Eikrem, K. S. & Nævdal, G. (2020) Target-oriented inversion of time-lapse seismic waveform data. *Communications in Computational Physics*, 28(1), 249–275.

Huang, X., Jakobsen, M. & Wu, R. (2020) On the applicability of a renormalized Born series for seismic wavefield modelling in strongly scattering media. *Journal of Geophysics and Engineering*, 17, 277–299.

Innanen, K. (2009) Born series forward modelling of seismic primary and multiple reflections: an inverse scattering shortcut. *Geophysical Journal International*, 177, 1197–1204.

Jakobsen, M. (2012) T-matrix approach to seismic forward modelling in the acoustic approximation. *Studia Geophysica et Geodaetica*, 56(1), 1–20.

Jakobsen, M., Huang, X. & Wu, R.-S. (2020) Homotopy analysis of the Lippmann-schwinger equation for seismic wavefield modelling in strongly scattering media. *Geophysical Journal International*, 222(2), 743–753.

Jakobsen, M. & Ursin, B. (2015) Full waveform inversion in the frequency domain using direct iterative T-matrix methods. *Journal of Geophysics and Engineering*, 12(3), 400–418.

Jakobsen, M. & Wu, R.-S. (2016) Renormalized scattering series for frequency-domain waveform modelling of strong velocity contrasts. *Geophysical Journal International*, 206(2), 880–899.

Jakobsen, M. & Wu, R.-S. (2018) Accelerating the T-matrix approach to seismic full-waveform inversion by domain decomposition. *Geophysical Prospecting*, 66(6), 1039–1059.

Jakobsen, M., Wu, R.-S. & Huang, X. (2020) Convergent scattering series solution of the inhomogeneous Helmholtz equation via renormalization group and homotopy continuation approaches. *Journal of Computational Physics*, 409, 109343.

Jiménez, A. A., Muñoz-Cuartas, J. C. & Avendaño, S. (2018) Integral modelling of propagation of incident waves in a laterally varying medium: an exploration in the frequency domain. *CTandF-Ciencia, tecnología y futuro*, 8(2), 33–45.

Keller, H. & Perozzi, D. (1983) Fast seismic ray tracing. *SIAM Journal on Applied Mathematics*, 43(4), 981–992.

Kwon, S. J. & Jeong, M. K. (1998) Ultrasound inverse scattering determination of speed of sound, density, and absorption. *IEEE Ultrasonics Symposium*, 2, 1631–1634.

Lavarello, R. J. & Oelze, M. L. (2009) Density imaging using inverse scattering. *The Journal of the Acoustical Society of America*, 125(2), 793–802.

Liao, S. (1997) Homotopy analysis method: a new analytical technique for nonlinear problems. *Communications in Nonlinear Science and Numerical Simulation*, 2, 95–100.

Liao, S. (2003) *Beyond Perturbation: Introduction to the Homotopy Analysis Method*. Boca Raton, FL: Chapman and Hall/CRC.

Liao, S. & Tan, Y. (2007) A general approach to obtain series solutions of nonlinear differential equations. *Studies in Applied Mathematics*, 119, 297–354.

Luo, J. & Wu, R.-S. (2018) Velocity and density reconstruction based on scattering angle separation. *Pure and Applied Geophysics*, 175(12), 4371–4387.

Malovichko, M., Khokhlov, N., Yavich, N. & Zhdanov, M. (2018) Acoustic 3D modeling by the method of integral equations. *Computers and Geosciences*, 111, 223–234.

Mavko, G., Mukerji, T. & Dvorkin, J. (2009) *The Rock Physics Handbook: Tools for Seismic Analysis of Porous Media, 2nd edition*. Cambridge: Cambridge University Press.

Mojabi, P. & LoVetri, J. (2015) Ultrasound tomography for simultaneous reconstruction of acoustic density, attenuation, and compressibility profiles. *The Journal of the Acoustical Society of America*, 137(4), 1813–1825.

Morse, P. M. & Feshbach, H. (1954) Methods of theoretical physics. *American Journal of Physics*, 22(6), 410–413.

Osnabrugge, G., Leedumrongwatthanakun, S. & Vellekoop, I. M. (2016) A convergent Born series for solving the inhomogeneous Helmholtz equation in arbitrarily large media. *Journal of Computational Physics*, 322, 113–124.

Rao, J., Yang, J., Ratassepp, M. & Fan, Z. (2020) Multi-parameter reconstruction of velocity and density using ultrasonic tomography based on full waveform inversion. *Ultrasonics*, 101, 106004.

Sun, M., Yang, J., Dong, L., Liu, Y. & Huang, C. (2017) Density reconstruction in multiparameter elastic full-waveform inversion. *Journal of Geophysics and Engineering*, 14(6), 1445–1462.

Van Den Berg, P. M. & Kleinman, R. E. (1997) A contrast source inversion method. *Inverse Problems*, 13(6), 1607.

Červený, V. (2005) *Seismic Ray Theory*. Cambridge: Cambridge University Press.

Virieux, J. & Operto, S. (2009) An overview of full-waveform inversion in exploration geophysics. *Geophysics*, 74(6), WCC1–WCC26.

Wu, R. & Zheng, Y. (2014) Non-linear partial derivative and its De Wolf approximation for non-linear seismic inversion. *Geophysical Journal International*, 196, 1827–1843.

Yang, J., Liu, Y. & Dong, L. (2016) Least-squares reverse time migration in the presence of density variations. *Geophysics*, 81(6), S497–S509.

Yao, J., Lesage, A.-C., Hussain, F. & Kouri, D. J. (2016) Forward scattering and Volterra renormalization for acoustic wavefield propagation in vertically varying media. *Communications in Computational Physics*, 20(2), 353–373.

Zhdanov, M. S. & Fang, S. (1997) Quasi-linear series in three-dimensional electromagnetic modeling. *Radio Science*, 32(6), 2167–2188.

APPENDIX

3D GREEN'S FUNCTION AND ITS SPATIAL DERIVATIVES

The three-dimensional acoustic Green's function for a homogeneous medium in the frequency domain can be expressed as (Červený, 2005)

$$G^{(0)}(\mathbf{r}, \omega) = \frac{1}{4\pi r} \exp(i\omega r/c_0), \tag{A1}$$

where

$$\mathbf{r} = \mathbf{x} - \mathbf{x}', \quad r = \|\mathbf{r}\|. \tag{A2}$$

For the convenience of derivation, we introduce the following notation:

$$A(r) = \frac{1}{4\pi} \exp(ar), \quad Z(r) = r, \quad a = i\omega/c_0. \tag{A3}$$

Equation (A1) can be rewritten as

$$G^{(0)}(r) = \frac{A(r)}{Z(r)}. \tag{A4}$$

From (A1)–(A4), we have

$$\nabla_{\mathbf{x}} G^{(0)} = \frac{\partial G^{(0)}}{\partial \mathbf{x}} = \frac{\partial G^{(0)}}{\partial r} \frac{\partial r}{\partial \mathbf{x}}, \tag{A5}$$

$$\frac{\partial A}{\partial r} = aA, \quad \frac{\partial Z}{\partial r} = 1, \tag{A6}$$

$$\frac{\partial G^{(0)}}{\partial r} = \frac{(\partial A/\partial r)Z - A(\partial Z/\partial r)}{Z^2} = \frac{aAZ - A}{Z^2}, \tag{A7}$$

$$r = \|\mathbf{r}\| = \sqrt{\mathbf{r}^{\mathsf{T}}\mathbf{r}} = \sqrt{l}, \tag{A8}$$

$$l = \mathbf{r}^{\mathsf{T}}\mathbf{r} = (\mathbf{x} - \mathbf{x}')^{\mathsf{T}}(\mathbf{x} - \mathbf{x}') = (\mathbf{x}^{\mathsf{T}}\mathbf{x} - 2\mathbf{x}^{\mathsf{T}}\mathbf{x}' + \mathbf{x}'^{\mathsf{T}}\mathbf{x}'), \tag{A9}$$

$$\frac{\partial l}{\partial \mathbf{x}} = 2(\mathbf{x} - \mathbf{x}') = 2\mathbf{r}, \quad \frac{\partial r}{\partial l} = \frac{1}{2r}, \tag{A10}$$

$$\frac{\partial r}{\partial \mathbf{x}} = \frac{\partial r}{\partial l} \frac{\partial l}{\partial \mathbf{x}} = \frac{1}{r}\mathbf{r}. \tag{A11}$$

By combining (A3), (A5), (A7) and (A11), we obtain the first spatial derivatives of $G^{(0)}$:

$$\nabla_{\mathbf{x}} G^{(0)}(\mathbf{r}, \omega) = A\left(\frac{a}{Z^2} - \frac{1}{Z^3}\right)\mathbf{r}$$
$$= \frac{1}{4\pi} \exp(i\omega r/c_0)\left(\frac{i\omega}{c_0 r^2} - \frac{1}{r^3}\right)\mathbf{r}. \tag{A12}$$

From (A12), we write the second spatial derivative of $G^{(0)}$ as

$$\nabla_{\mathbf{x}}\nabla_{\mathbf{x}} G^{(0)} = \frac{\partial}{\partial \mathbf{x}}\left(\frac{\partial G^{(0)}}{\partial \mathbf{x}}\right) = \left[a\frac{\partial}{\partial \mathbf{x}}\left(\frac{A}{Z^2}\mathbf{r}\right) - \frac{\partial}{\partial \mathbf{x}}\left(\frac{A}{Z^3}\mathbf{r}\right)\right]. \tag{A13}$$

According to (A2), we derive

$$\frac{\partial \mathbf{r}}{\partial \mathbf{x}} = \mathbf{I}_3, \tag{A14}$$

where $\mathbf{I}_3$ is a $3{\times}3$ identity matrix. In (A13), we have

$$\frac{\partial}{\partial \mathbf{x}}\left(\frac{A}{Z^2}\mathbf{r}\right) = \frac{\partial}{\partial \mathbf{x}}\left(\frac{A}{Z^2}\right)\mathbf{r} + \frac{A}{Z^2}\frac{\partial \mathbf{r}}{\partial \mathbf{x}}$$

$$= \frac{aAZ^2 - 2AZ}{Z^4}\frac{\partial r}{\partial \mathbf{x}}\mathbf{r} + \frac{A}{Z^2}\mathbf{I}_3, \tag{A15}$$

$$\frac{\partial}{\partial \mathbf{x}}\left(\frac{A}{Z^3}\mathbf{r}\right) = \frac{\partial}{\partial \mathbf{x}}\left(\frac{A}{Z^3}\right)\mathbf{r} + \frac{A}{Z^3}\frac{\partial \mathbf{r}}{\partial \mathbf{x}}$$

$$= \frac{aAZ^3 - 3AZ^2}{Z^6}\frac{\partial r}{\partial \mathbf{x}}\mathbf{r} + \frac{A}{Z^3}\mathbf{I}_3. \tag{A16}$$

By combing (A3), (A13), (A15) and (A16), we obtain the second spatial derivatives of $G^{(0)}$:

$$\nabla_\mathbf{x}\nabla_\mathbf{x}G^{(0)}(\mathbf{r}, \omega) = A\left[\left(\frac{a^2}{Z^3} - \frac{3a}{Z^4} + \frac{3}{Z^5}\right)\mathbf{r}\mathbf{r}^\mathsf{T} + \left(\frac{a}{Z^2} - \frac{1}{Z^3}\right)\mathbf{I}_3\right]$$

$$= \frac{1}{4\pi}\exp(i\omega r/c_0)\left[\left(-\frac{\omega^2}{c_0^2 r^3} - \frac{3i\omega}{c_0 r^4} + \frac{3}{r^5}\right)\mathbf{r}\mathbf{r}^\mathsf{T}\right.$$

$$\left. + \left(\frac{i\omega}{c_0 r^2} - \frac{1}{r^3}\right)\mathbf{I}_3\right]. \tag{A17}$$

2D GREEN'S FUNCTION AND ITS SPATIAL DERIVATIVES

The two-dimensional Green's function for a homogeneous acoustic medium is (Červený, 2005)

$$G_{2D}^{(0)}(\mathbf{r}, \omega) = \frac{1}{4}iH_0^{(1)}(\omega r/c_0), \tag{B1}$$

where

$$\mathbf{r} = \mathbf{x} - \mathbf{x}', \quad r = \|\mathbf{r}\| \tag{B2}$$

and $H_0^{(1)}$ is the Hankel function of the first kind and zeroth order. The Hankel function has the recurrence relation (Arfken and Weber, 1999):

$$\frac{\partial H_0^{(1)}(x)}{\partial x} = -H_1^{(1)}(x), \quad \frac{\partial^2 H_0^{(1)}(x)}{\partial x^2} = -H_0^{(1)}(x) + \frac{H_1^{(1)}(x)}{x}. \tag{B3}$$

We introduce a new notation:

$$Z(r) = \omega r/c_0. \tag{B4}$$

From (B2), we derive

$$\frac{\partial r}{\partial \mathbf{x}} = \frac{1}{r}\mathbf{r}, \quad \frac{\partial \mathbf{r}}{\partial \mathbf{x}} = \mathbf{I}_2, \tag{B5}$$

where $\mathbf{I}_2$ is a $2{\times}2$ identity matrix.

According to the chain rule and (B1)–(B5), we get

$$\nabla_\mathbf{x}G_{2D}^{(0)}(\mathbf{r}, \omega) = \frac{\partial G_{2D}^{(0)}}{\partial \mathbf{x}} = \frac{\partial G_{2D}^{(0)}}{\partial H}\frac{\partial H}{\partial Z}\frac{\partial Z}{\partial r}\frac{\partial r}{\partial \mathbf{x}}$$

$$= -\frac{i\omega}{4c_0 r}H_1^{(1)}(\omega r/c_0)\mathbf{r}. \tag{B6}$$

Through (B5), we obtain

$$\frac{\partial^2 r}{\partial \mathbf{x}^2} = \frac{\partial}{\partial \mathbf{x}}\left(\frac{\partial r}{\partial \mathbf{x}}\right) = \frac{\partial}{\partial \mathbf{x}}\left(\frac{\mathbf{r}}{r}\right) = \frac{(\partial \mathbf{r}/\partial \mathbf{x})r - \mathbf{r}(\partial r/\partial \mathbf{x})}{r^2}$$

$$= \frac{1}{r}\left(\mathbf{I}_2 - \frac{1}{r^2}\mathbf{r}\mathbf{r}^\mathsf{T}\right). \tag{B7}$$

By using the chain rule and (B3)–(B7), we have

$$\nabla_\mathbf{x}\nabla_\mathbf{x}G_{2D}^{(0)}(\mathbf{r}, \omega) = \frac{\partial}{\partial \mathbf{x}}\left(\frac{\partial G_{2D}^{(0)}}{\partial \mathbf{x}}\right) = \frac{i\omega}{4c_0}\frac{\partial}{\partial \mathbf{x}}\left(\frac{\partial H}{\partial Z}\frac{\partial r}{\partial \mathbf{x}}\right) = \frac{i\omega}{4c_0}\left(\frac{\partial^2 H}{\partial Z^2}\frac{\partial Z}{\partial r}\frac{\partial r}{\partial \mathbf{x}}\frac{\partial r}{\partial \mathbf{x}} + \frac{\partial H}{\partial Z}\frac{\partial^2 r}{\partial \mathbf{x}^2}\right)$$

$$= \frac{i\omega}{4c_0}\left\{-\frac{1}{r}H_1^{(1)}(Z)\mathbf{I}_2 + \left[\frac{\omega}{c_0 r^2}\left(-H_0^{(1)}(Z) + \frac{H_1^{(1)}(Z)}{Z}\right) + \frac{1}{r^3}H_1^{(1)}(Z)\right]\mathbf{r}\mathbf{r}^\mathsf{T}\right\} \tag{B8}$$

$$= \frac{i\omega}{4c_0}\left\{-\frac{1}{r}H_1^{(1)}(\omega r/c_0)\mathbf{I}_2 + \left[-\frac{\omega}{c_0 r^2}H_0^{(1)}(\omega r/c_0) + \frac{2}{r^3}H_1^{(1)}(\omega r/c_0)\right]\mathbf{r}\mathbf{r}^\mathsf{T}\right\}.$$